Visualization of Clouds and Atmospheric Air Flows

Noël Rimensberger* Markus Gross† Tobias Günther‡

Computer Graphics Laboratory, ETH Zürich

ABSTRACT

Cloud dynamics play an essential role in meteorology. With the increase of computational power and due to the recent advances in cloud modeling, numerical simulations become available that include cloud evolution and precipitation processes at an unprecedented level of detail. This paper summarizes our analysis of the atmospheric cloud, rain and wind data that was provided for the IEEE Scientific Visualization Contest 2017. We provide overview visualizations of the individual attributes and analyze certain subregions in more detail. Among others, we observe vorticity and divergence near the tropopause, render unbiased images of hyperbolic Lagrangian coherent structures, study the influence of topography, visualize takeoff and landing directions of airplanes, compare different data resolutions and present a 3D cloud classification algorithm.

1 INTRODUCTION

The 2017 IEEE Scientific Visualization Contest [13] addresses the arising challenges in the visualization and analysis of atmospheric cloud-resolving simulations. In this paper, we describe our findings on the various tasks contained in the contest, including the general tasks, the tasks from group A and selected tasks from groups B and C. We utilize direct and indirect ways to represent scalar atmospheric attributes such as cloud water content or air pressure, and employ Eulerian and Lagrangian techniques for air flow visualization. Since an accurate classification of clouds is helpful for weather forecasting and for the improvement of weather models, we present a 3D cloud classification based on two common classification schemes [6, 14].

Aside from the overviews that cover entire Germany, we focus the analysis on two regions of interests, which experienced interesting weather situations. The first region is around Regensburg in Bavaria, which we call the *updraft* region. April 26^{th} 2013 was the hottest day in Regensburg in all April, but was also a turning point [12]. From 25^{th} to 27^{th}, the air pressure dropped by $23 hPa$, which marks the arrival of a low pressure area. From 26^{th} to 28^{th}, the maximum day temperature decreased from $27°C$ to $12°C$. On April 26^{th}, we observe strong updraft and cloud development in the simulation, which might be caused by the high surface temperature.

The second region is around Paderborn, which is near Teutoburg Forest (Teutoburger Wald) and the Egge Hills (Eggegebirge), which we later refer to as the *mountain* region [11]. From April 25^{th} to 26^{th}, the temperature decreased from $20°C$ to $7°C$ degrees, while the air pressure dropped by $12 hPa$. The updrafts and cloud dynamics in this region are influenced by the topography, as we will show later.

2 DATA PREPROCESSING

Most of our visualizations are based on the four hour time series of the lon/lat data set. To ease the data handling and to facilitate the work with consumer hardware, we split the data into smaller chunks. We prepared a single VTK ImageData (.vti) file for each attribute and per time step. The complete region was down-sampled and selected regions of interested were extracted from the original rectilinear grid. The resulting extents, the respective resolutions and the corresponding file sizes are shown in Table 1. For each region of interest and for each attribute a total of 240 files with the temporal resolution of 1 minute was prepared.

Region	Extent			Resolution			File size	
	Lon (°)	Lat (°)	Height (*m*)	x	y	z	2D	3D
Complete	[4.5, 14.5]	[47.5, 54.5]	[107, 20800]	286	311	150	356 KB	53 MB
Updraft	[11.1, 13.3]	[48.3, 50.1]	[107, 20800]	315	401	150	506 KB	76 MB
Mountains	[7, 9.2]	[50.9, 52.5]	[107, 5870]	316	357	70	452 KB	32 MB

Table 1: Spatial extent, resolution and file size of a single time step per attribute for each prepared region of interest.

The *complete* region covers the entirety of Germany. The *updraft* region is located around Regensburg and shows this smaller region at higher resolution. The *mountain* region extents around the forested hills Teutoburg Forest (Teutoburger Wald) and the Egge Hills (Eggegebirge) in the state of North Rhine-Westphalia.

Fig. 1 shows the extents of the selected regions on the map of Germany. Additionally, an overview of the present weather conditions is given, with a weather map that is based on the given contest data and historic weather reports [11, 12].

3 VISUALIZATIONS

The provided data shows the weather situation above Germany for April 26, 2013 from 17:00 to 21:00. The given spatial and temporal domain contains several interesting phenomena that we elaborate on in this section. First, rain bands and thick clouds across Germany dominate the picture, with one separated rain cloud in the south-east. This aside, turbulence at different locations and in varying altitudes can be observed. Following the proposed tasks, we look at several of these interesting situations, and thereby, utilize multiple visualization techniques.

3.1 General Visualizations

Clouds, Rain and Ice

First, we look at the general cloud and rain properties: cloud water content (CLW), cloud ice content (CLI) and rain mixing ratio (QR). Fig. 2 shows an overview of various visualizations, helping in the investigation of the present weather situation. Cloud water content is visualized with a volume rendering in Fig. 2a. The top view resembles a photo-realistic appearance as known from satellite images, which makes it intuitive to read. Both cloud cover and cloud thickness can be seen, while cloud height is only perceivable to some degree with the help of the tilted view.

To improve the altitude visualization, we visualize iso-surfaces of the cloud water content and map air pressure values to color in Fig. 2b. The CLW-isovalue ($CLW = 4 \times 10^{-4}\,\mathrm{kg\,kg^{-1}}$) cuts off cloud boundaries and minor clouds with low cloud water content. As a result, distinguishable and separated cloud structures appear instead of one big cloud body. As air pressure decreases almost

*e-mail: noelr@ethz.ch

†e-mail: grossm@inf.ethz.ch

‡e-mail: tobias.guenther@inf.ethz.ch

linearly with increasing altitude, it is a helpful indicator of height that can complement direct altitude visualization. Thus with this colouring, the height of the cloud top becomes visible in the top view, producing cloud layers that are distinguishable by air pressure. Additionally, vertical extents are visible in the tilted view.

The cloud water content (CLW), cloud ice content (CLI) and the rain mixing ratio (QR) are visualized in Fig. 2c using isosurfaces. The tilted view provides an impression of the vertical stacking of the different water-related fields, their spatial extent and coverage.

As iso-surfaces do not depict minima or maxima, we choose different techniques to visualize rain bands and rain quantities. Fig. 2d shows the total precipitable water per column vertically integrated and thus projected into 2D on the left. The resulting precipitation map resembles known weather forecasts and radar images. Similar insights can be gained by the volume rendering of the rain mixing ratio (QR) values on the right. Again, the rain clouds that develop around Regensburg in the south-east of Germany are visible in both visualizations due to a strong precipitation in a small area.

Airplane Trajectories

We investigate the possible effects of the severe weather conditions on the flight paths in two ways. The visualization of flight paths in Fig. 3 allows us to directly look for deviations in the spatial domain. Multiple flights take off eastwards from Frankfurt am Main straight through thick clouds with rainfall. One flight from Munich starts into the direction of the thick visible rain clouds. A slight curve around the cloud center is recognisable. Though without data on original flight plans, we can only assume a deviation from the original path.

A more analytical approach is shown in Fig. 4. We study two of the bigger airports, Munich and Frankfurt, which are partially surrounded by severe weather conditions. The takeoff and landing directions throughout the day are plotted. From the preceding insights on the weather situation we could suspect runway changes around 19:00. But the figures show no clear evidence of any adjustments during the day. We conclude that the existing weather conditions were not severe enough for major adaptions.

3.2 Visualization of Wind

Vorticity and Divergence

For a given time-dependent 3D wind velocity field $\mathbf{v}(x,y,z,t) = (u(x,y,z,t), v(x,y,z,t), w(x,y,z,t))^{\mathrm{T}}$, a first approach is to study wind by Eulerian visualizations of derived differential properties such as vorticity magnitude $\|\nabla \times \mathbf{v}\|$ and horizontal divergence $\nabla \cdot \mathbf{v} = \frac{\partial u}{\partial x} + \frac{\partial v}{\partial y}$. Fig. 5a shows a direct volume rendering of the vorticity magnitude. Vorticity maxima appear near the ground due to boundary-induced shear, and at higher altitude around $10\,km$. The high layers of vorticity can be an indication for the tropopause, which is the boundary layer between troposphere and stratosphere. Here, wind shear may lead to clear air turbulence (CAT) and vortices [9].

The volume rendering of horizontal divergence in Fig. 5b looks more scattered. Two interesting spots in the south-east of Germany are highlighted. In both regions we see clouds with high convergence near the ground and high divergence at higher levels. This is expected around vertically developed clouds with high updrafts.

In Fig. 5c, the relationship between clouds and vorticity is studied for the *updraft* region in south-east Germany. Here, vorticity iso-surfaces are shown in combination with a precipitation map on the ground, as well as CLW and CLI isosurfaces that depict clouds. We see high values of vorticity developing at the top of the cumulonimbus cloud system. We will further discuss this phenomenon in the following paragraph on pathlines.

To differentiate between orography induced circulation and turbulence in clouds, we visualize the divergence using iso-surfaces in Fig. 5d. What cannot easily be seen on a steady image but rather on the accompanying video is that there are two types of occurrences of high divergence. First, we see high divergence following the updrafts, and second, there are steady clusters around hill ranges, as highlighted in west Germany. One example of orography induced turbulence is discussed in more detail in the following paragraph.

Atmospheric Trajectories

We additionally provide a Lagrangian view on the wind data using pathlines. A pathline is the trajectory that a massless tracer particle follows in an unsteady vector field. In Fig. 6, we focus on the updraft and the turbulence around the cumulonimbus system in south-east Germany. We depict pathlines with an integration duration of 20 minutes, starting at the cloud bottom. Most trajectories reach high altitudes due to updrafts, traveling from the cloud bottom to the top, where they flatten out and spread. The updraft is fairly turbulent with high vorticity values at different altitudes. To give an overview of all pathlines, we provide a focus and context visualization in Fig. 7. Using decoupled opacity optimization [3], we fade out occluding pathlines that hinder the view on lines with high updraft.

An interesting phenomenon can be seen at the top of the cloud: Fig. 8 shows a progression over time of pathlines coloured by vorticity at the top of the cloud. As the rain clouds are passing by the seeding region, we can see high vorticity and turbulence from the colouring as well as from the lines themselves. Before and after the clouds arrive, two streaks of high vorticity are noticeable, both arising from the wind shear at the height levels. Air masses moving with different speeds are visualized by the varying pathline lengths. The vorticity maxima are directly at the boundaries between those air masses, indicating shear-induced vorticity. Air masses moving with different speed can be an indication of the tropopause.

Fig. 9 visualizes the orography-induced turbulence and compression at the luv side of the the Teutoburg Forest and the Egge Hills. Winds coming from west are forced upwards by the mountains and we can see an example of cloud formation due to orographic lift.

Hyperbolic Lagrangian Coherent Structures

Finite-time Lyapunov exponents (FTLE) are a frequently used indicator for hyperbolic Lagrangian coherent structures, which act as transport barriers of tracer particles [4]. The FTLE field is a Lagrangian measure that exhibits extremely thin ridge structures, which is why we used an unbiased Monte Carlo rendering approach [2] to visualize the transport barriers. Fig. 10 shows the ground-induced turbulence, updraft columns and transport barriers at the tropopause for entire Germany and a selected region of interest around Regensburg. Ground turbulence is apparent particularly in the south (due to the Alps) and generally in the southern and eastern part of Germany. A comparison with Fig. 2a depicts the reason: in the south, sun light reaches the ground, causing a temperature-induced convection, paired with turbulence due to the arrival of a low pressure area.

3.3 Comparing Resolutions

The sheer size of the high resolution data, especially in 3D, raises the question whether it is worth the additional computational effort. Using the 2D ICON data with different resolutions, we computed difference maps, which are shown in Fig. 11. We see considerable differences between the finest (Domain 3) and the coarsest (Domain 1) scale. The differences are particularly large for non-integrated (local) attributes such as air pressure or cloud cover. Note that for those, the differences are larger at the cloud bottom than at the cloud top. We observed smaller differences for altitude-integrated attributes, such as CLWVI and CLIVI. Generally, we found that the most significant differences occurred at the boundaries of the clouds.

In Fig. 12, the mid resolution (Domain 2) is compared, as well. While visually better than Domain 1, cloud boundaries still show significant deviations. We would consider Domain 2 to be sufficient for most analysis tasks. High resolution data is required for the extraction of cloud boundaries and when local properties are concerned, but it is less important for altitude-integrated measures.

3.4 Cloud Classification

Finally, after the detailed study of various visualizations, we present the results of two cloud classification schemes. The first scheme follows the World Meteorological Organization's *International Cloud Atlas* [14]. It mainly works with geometrical cloud height and altitude. Aside from low level, mid level and high level clouds, two types of vertically developed clouds are distinguished: nimbostratus (Ns) and cumulonimbus (Cb). In addition to height information, precipitation is taken as indicator for Ns or Cb clouds.

The second approach is based on the classification scheme by the International Satellite Cloud Climatology Project (ISCCP) [6] and distinguishes nine cloud types. The scheme used by the ISCCP works for satellite imagery and depends on cloud optical thickness τ, which is a measure of the attenuation of light passing through a cloud. Stephens [10] shows that the cloud optical thickness is closely related to the liquid water path (LWP) of a cloud. The LWP is the amount of liquid water between two points, in this particular case between cloud bottom z_0 and cloud top z_1. It is defined as

$$\mathrm{LWP} = \int_{z_0}^{z_1} \rho_{air} \cdot \mathrm{CLW}\,\mathrm{d}z \ , \tag{1}$$

where ρ_{air} is the density of air. The density of *dry air* is

$$\rho_{air} = \frac{p}{T \cdot R_{specific}} \ , \tag{2}$$

where $R_{specific} = 287.058\,\mathrm{J}/(\mathrm{kg}\cdot\mathrm{K})$ is the specific gas constant of dry air, p is the air pressure (given as PRES) and T is the air temperature (given as TA). To get the density of *humid air*, we compute the virtual temperature T_v that a dry air mass would have in order to have the same density as humid air at temperature T, cf. Erneis [1]:

$$T_v = T \cdot (1 + 0.609\,q) \tag{3}$$

where q is the specific humidity (given as HUS). The cloud optical thickness τ is then estimated using Stephens' relation [10]:

$$\log_{10}(\tau) \approx 0.2633 + 1.7095 \log_e(\log_{10}(\mathrm{LWP})). \tag{4}$$

Before clouds can be classified, they have to be detected. For this, we iterate over vertical columns in the atmosphere and look for vertically connected cloud components. A threshold on the cloud water content ($CLW = 1 \times 10^{-10}\,\mathrm{kg\,kg^{-1}}$) is used to determine whether a cloud is present or not. This way, multiple cloud layers can be distinguished within a single column. In contrast to common classification approaches working on satellite imagery, we can thus detect clouds which otherwise would stay hidden. For each of those layers, we then determine the necessary properties such as geometrical cloud height, cloud top pressure or liquid water path which we later use for the actual classification. Each vertically connected cloud layer is classified by one of the approaches described above.

The resulting classifications are shown in Fig. 13. Both visualizations show small fluctuations in the horizontal direction, due to the fact that horizontal connectivity is not considered. For the basic cloud levels, the two approaches agree in most parts, but a significant difference is seen in the classification of the Cb and Ns clouds. In general, what the first approach classifies as Ns clouds, the ISCCP approach classifies as altocumulus (Ac) clouds. This is most probably due to the fact that these cloud regions do have precipitation, which is considered as indicator for Ns in the first approach, but does not have an influence in the second approach. Apart from that, both pictures generally agree with each other and with the preceding insights. A 3D visualization is shown in Fig. 14.

4 Implementation

We built an interactive visualization tool based on VTK [8] and Qt5 [7]. The pathlines are integrated using a fourth-order Runge-Kutta integrator with a step size of 5 seconds. Since the time steps for the 3D data is 1 minute, the wind fields have to be interpolated for the integration. We compute the pathlines with corresponding vorticity and divergence values on the fly to allow for an interactive exploration of the data. A seeding box can be moved and the pathlines can be coloured by vorticity, horizontal divergence or the updraft. For the colouring, we use color maps from ColorBrewer [5]. Our system is equipped with an Intel Core i7 with 2.3 GHz, 16 GB RAM and an NVIDIA GeForce GT 650M with 512 MB VRAM. The available RAM allows for the computation of pathlines with lengths up to 30 minutes. The computation and rendering of 1000 pathlines with a length of 20 minutes takes 2.1 seconds on the highest resolution grid used with 20 million points. The two FTLE visualizations in Fig. 10 were computed on an Nvidia GTX 970 GPU within 7 days (6000 samples per pixel for entire Germany) and 5 days (2000 samples per pixel for Regensburg), respectively.

5 Conclusion

We visualized the weather situation above Germany on April 26, 2013. We showed CLW, CLI and QR for the entire domain, which were viewed in the presence of air plane trajectories. For the wind visualizations, we concentrated on orography-induced cloud development and updraft, which we related to divergence and vorticity. We compared different ICON resolutions and to better understand the Lagrangian processes, we employed unbiased FTLE rendering and decoupled opacity optimization. Finally, we extended two 2D cloud classifications to 3D.

In the future, we would like to advance the classification methods by improving spatial smoothness and temporal coherence. Visualizing the differences between historically measured attributes and the reanalysis simulation is an interesting avenue for future work.

References

[1] S. Erneis. *Wind Energy Meteorology: Atmospheric Physics for Wind Power Generation*. Springer, 2013. doi: 10.1007/978-3-642-30523-8

[2] T. Günther, A. Kuhn, and H. Theisel. MCFTLE: Monte Carlo rendering of finite-time Lyapunov exponent fields. *Computer Graphics Forum (Proc. EuroVis)*, 35(3):381–390, 2016.

[3] T. Günther, H. Theisel, and M. Gross. Decoupled opacity optimization for points, lines and surfaces. *Computer Graphics Forum (Proc. Eurographics)*, 36(2):153–162, 2017.

[4] G. Haller. Distinguished material surfaces and coherent structures in three-dimensional fluid flows. *Physica D: Nonlinear Phenomena*, 149(4):248–277, Mar. 2001. doi: 10.1016/S0167-2789(00)00199-8

[5] M. Harrower and C. A. Brewer. Colorbrewer.org: An online tool for selecting colour schemes for maps. *The Cartographic Journal*, 40(1):27–37, 2003. doi: 10.1179/000870403235002042

[6] International satellite cloud climatology project. `https://isccp.giss.nasa.gov/cloudtypes.html`. Accessed: 2017-07-16.

[7] Qt. `https://www.qt.io`. Accessed: 2017-07-16.

[8] W. Schroeder, K. Martin, and B. Lorensen. *The Visualization Toolkit*. Kitware, 4 ed., 2006.

[9] M. A. Shapiro. Turbulent mixing within tropopause folds as a mechanism for the exchange of chemical constituents between the stratosphere and troposphere. *Journal of the Atmospheric Sciences*, 37(5):994–1004, 1980. doi: 10.1175/1520-0469(1980)037<0994:TMWTFA>2.0.CO;2

[10] G. L. Stephens. Radiation profiles in extended water clouds. ii: Parameterization schemes. *Journal of the Atmospheric Sciences*, 35(11):2123–2132, 1978. doi: 10.1175/1520-0469(1978)035<2123:RPIEWC>2.0.CO;2

[11] Weather station Bad Lippspringe. `http://www.wetteronline.de/rueckblick?gid=10430`. Accessed: 2017-07-16.

[12] Weather station Regensburg/Oberhub. `http://www.wetteronline.de/rueckblick?gid=10776`. Accessed: 2017-07-16.

[13] T. Wischgoll and A. Chourasia. IEEE Scientific Visualization Contest 2017. `https://www.dkrz.de/SciVis`. Accessed: 2017-07-16.

[14] World Meteorological Organization. *International Cloud Atlas, Vol. I*. WMO, 1975.

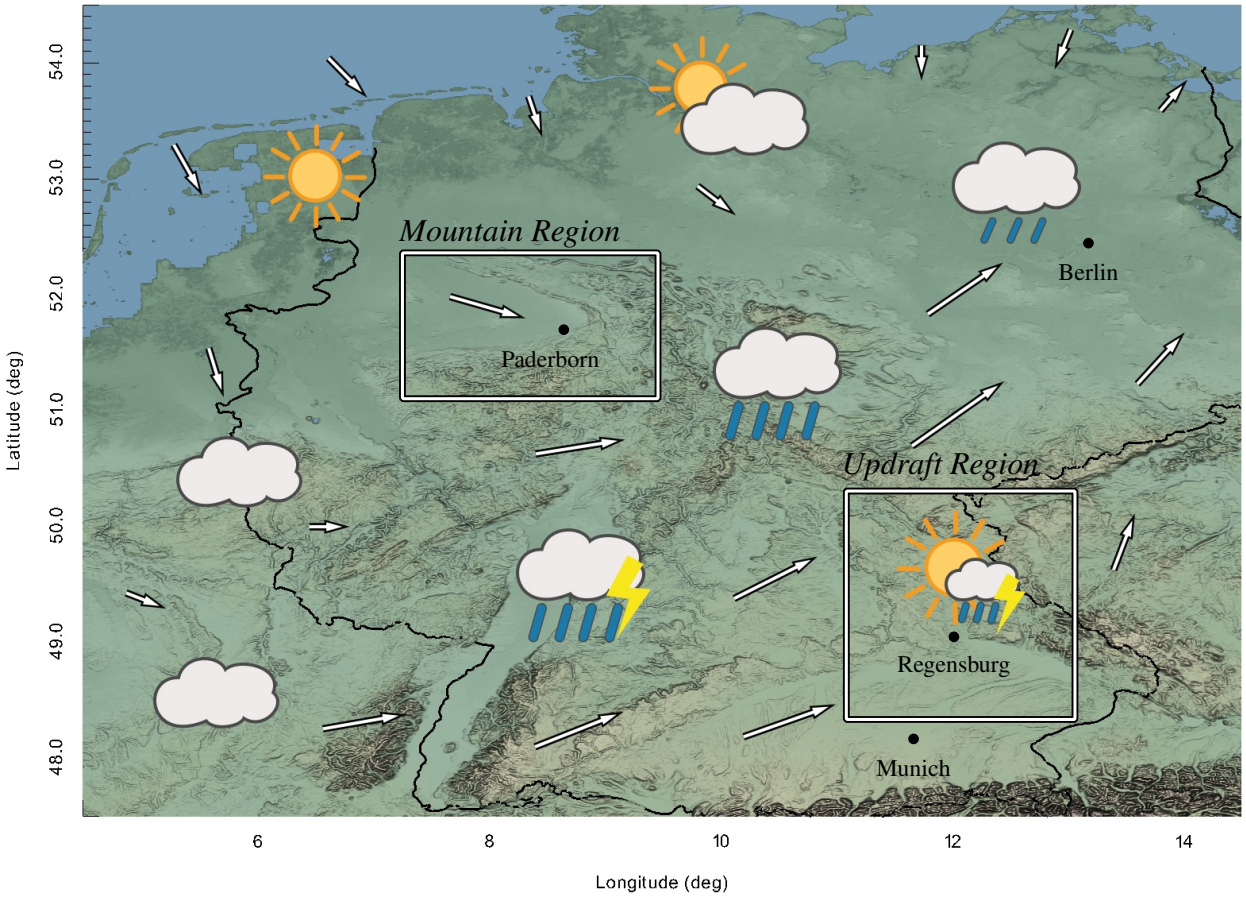

Figure 1: This figure shows an overview of the present weather conditions in the evening (19:00) of April 26, 2013. The glyphs provide an approximate depiction based on actual weather reports at that time [11, 12]. We highlighted the two regions of interest (*mountain region* and *updraft region*), which we discuss in more detail in the remainder of the paper. As shown later, the contest simulation data resembles these weather reports closely.

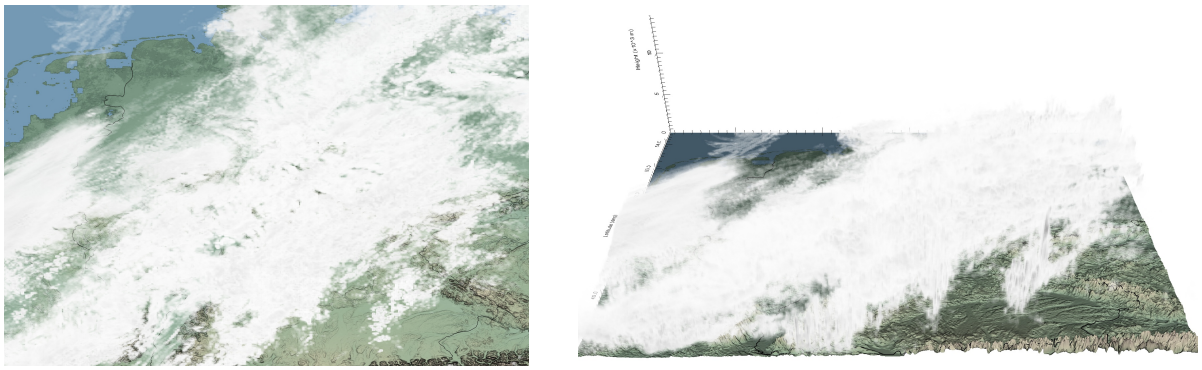

(a) Direct volume rendering of the cloud water content (CLW) from a top view (left) and a tilted view (right) at Germany.

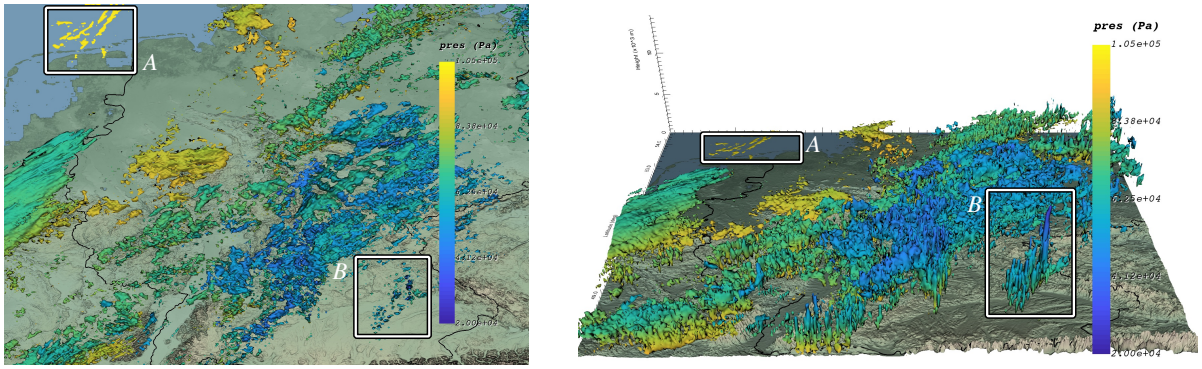

(b) Mapping air pressure to colour on the CLW iso-surfaces ($CLW = 4 \times 10^{-4}\,\mathrm{kg\,kg^{-1}}$) provides additional altitude-related information. For instance, the colour mapping allows us to easier distinguish low-lying fog (*A*) from vertically developed clouds (*B*).

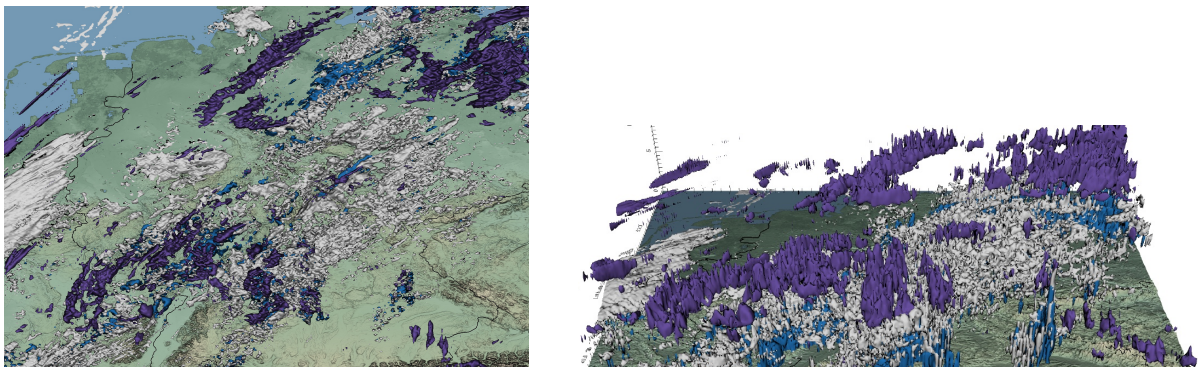

(c) Iso-surfaces of CLW (white), CLI (violet) and QR (blue) display the various types of water content in the atmosphere and how they are typically stacked by altitude, here with the thresholds: $CLW = 4 \times 10^{-4}\,\mathrm{kg\,kg^{-1}}$, $CLI = 1.5 \times 10^{-4}\,\mathrm{kg\,kg^{-1}}$ and $QR = 1 \times 10^{-4}\,\mathrm{kg\,kg^{-1}}$.

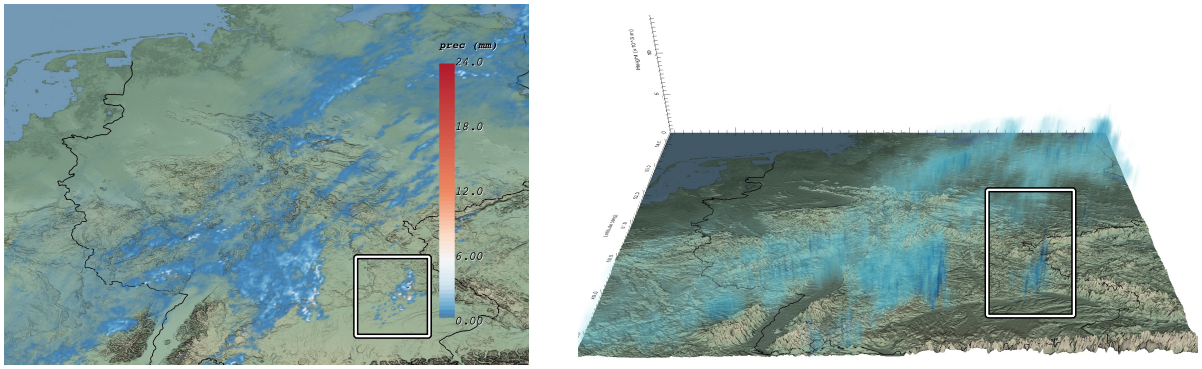

(d) Precipitation as 2D projection of QR values (left) and as volume rendering (right). Note that the *updraft* region around Regensburg shows strong and localized precipitation.

Figure 2: To provide an overview, this figure shows various cloud and rain attributes at 19:00 over the whole spatial domain of Germany. The volume renderings of CLW in Fig. 2a resemble familiar satellite imagery and give a sense of cloud cover and thickness. An improved view on cloud levels and geometrical height is given in Fig. 2b using the air pressure as colour map on CLW iso-surfaces. Displaying CLW, CLI and QR isosurfaces in Fig. 2c shows their relative order by altitude. Finally, Fig. 2d displays the amount of rain, which reveals maxima.

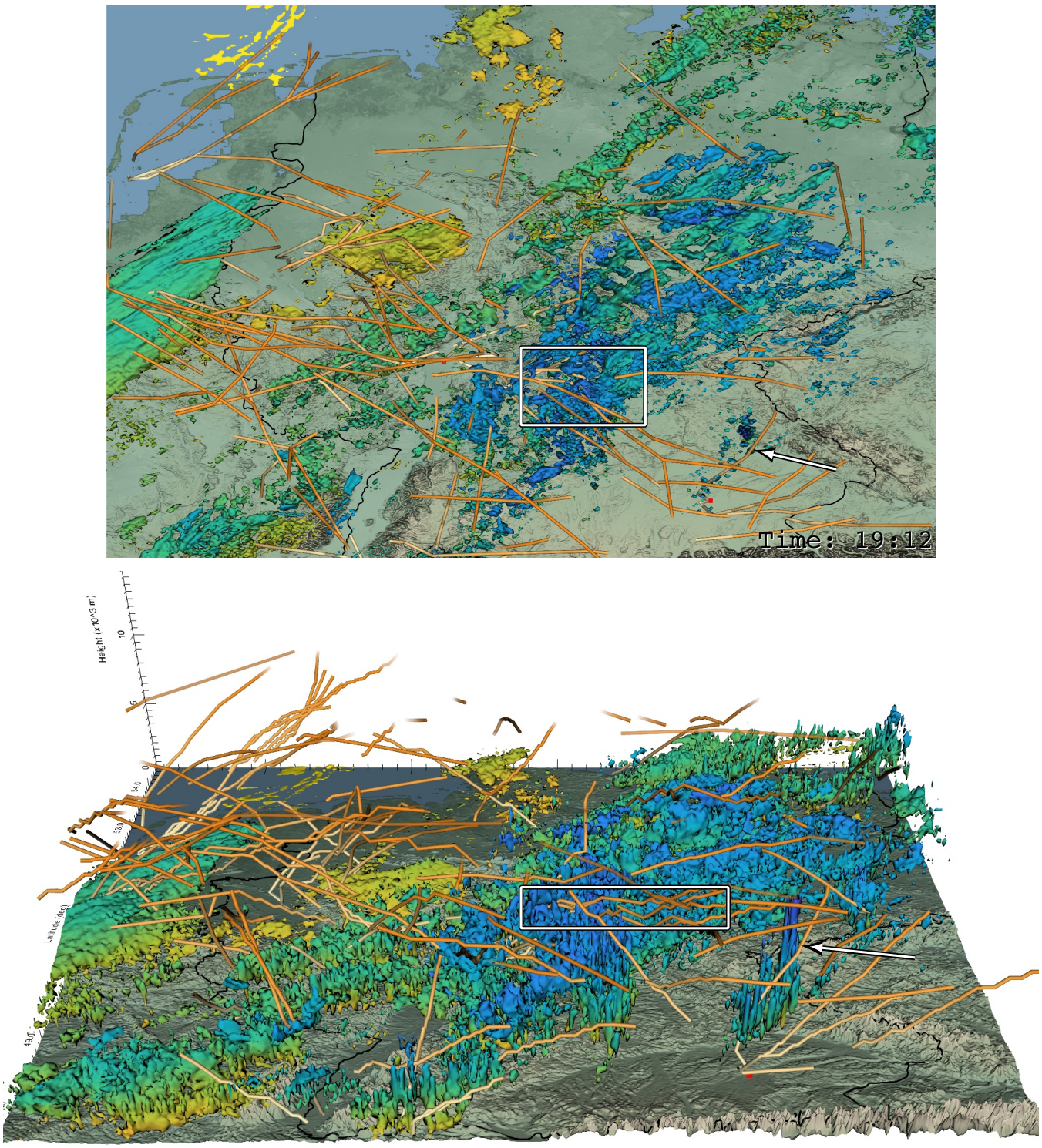

Figure 3: Here, all flight trajectories below 10 *km* are shown with the trajectories ranging from 19:00 to 19:12. The region that is marked with a rectangle shows takeoffs from Frankfurt going through vertically developed clouds. The arrow points to one flight from Munich slightly curving around the cumulonimbus cloud system at Regensburg.

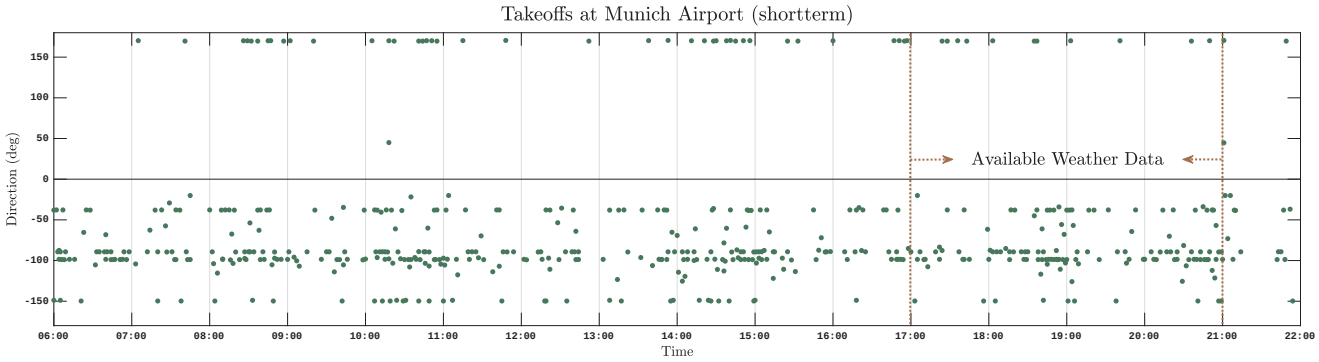
Takeoffs at Munich Airport (shortterm)
Direction (deg)
150
100
50
0
-50
-100
-150
Available Weather Data
06:00
07:00
08:00
09:00
10:00
11:00
12:00
13:00
14:00
15:00
16:00
17:00
18:00
19:00
20:00
21:00
22:00
Time

(a)

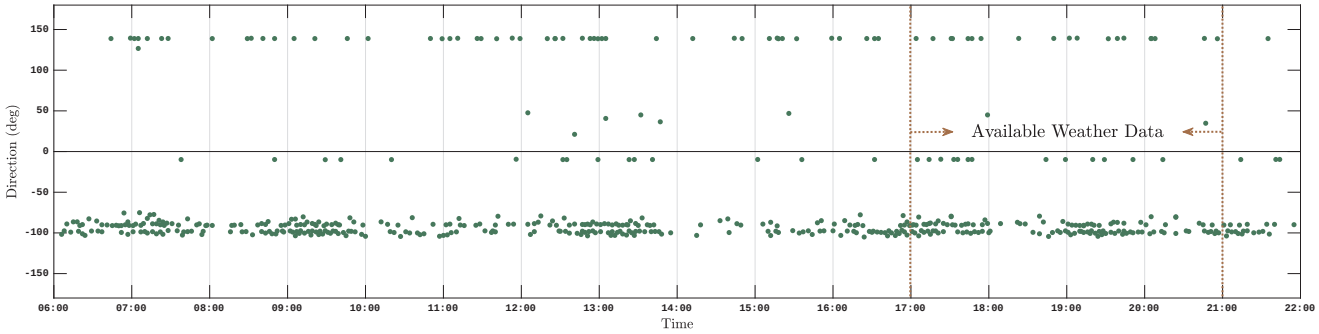
Landings at Munich Airport (shortterm)
Direction (deg)
150
100
50
0
-50
-100
-150
Available Weather Data
06:00
07:00
08:00
09:00
10:00
11:00
12:00
13:00
14:00
15:00
16:00
17:00
18:00
19:00
20:00
21:00
22:00
Time

(b)

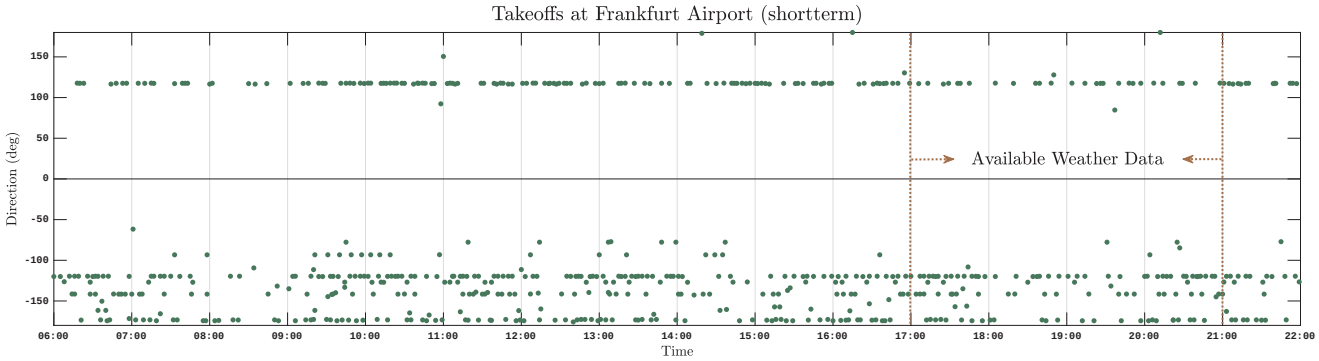
Takeoffs at Frankfurt Airport (shortterm)
Direction (deg)
150
100
50
0
-50
-100
-150
Available Weather Data
06:00
07:00
08:00
09:00
10:00
11:00
12:00
13:00
14:00
15:00
16:00
17:00
18:00
19:00
20:00
21:00
22:00
Time

(c)

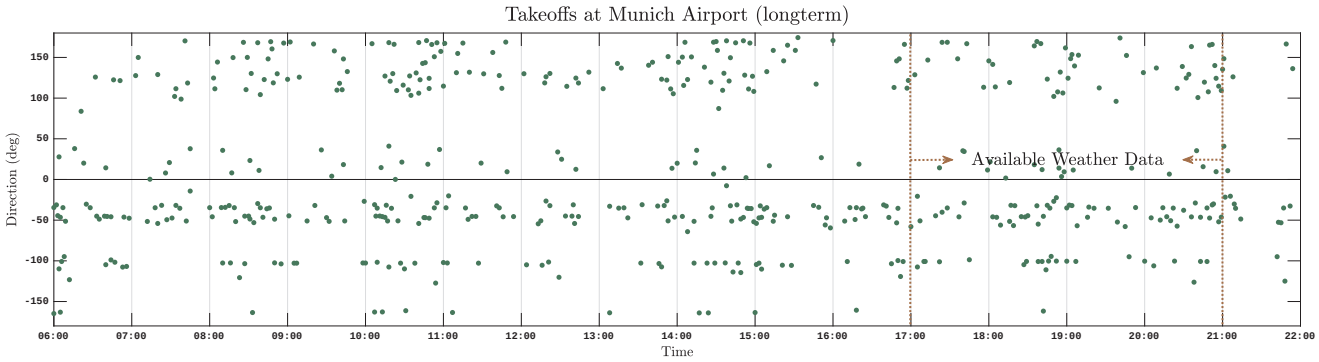

(d)

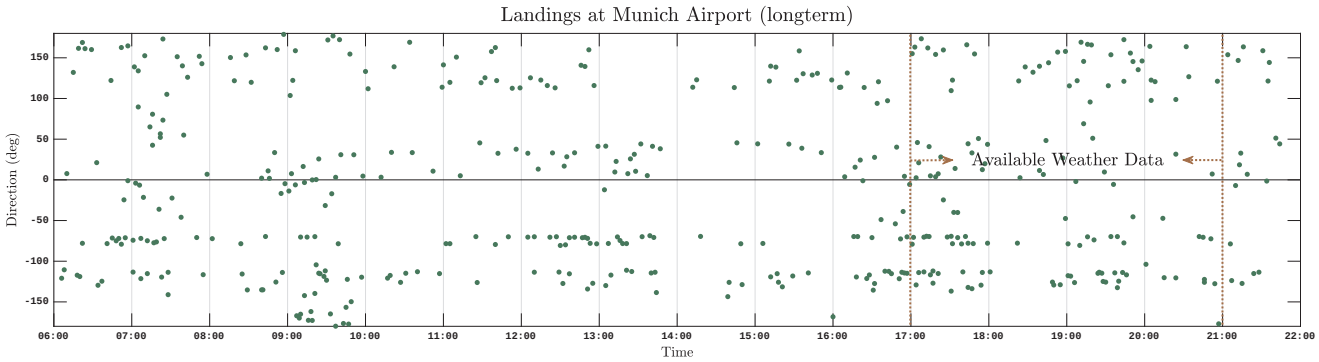

(e)

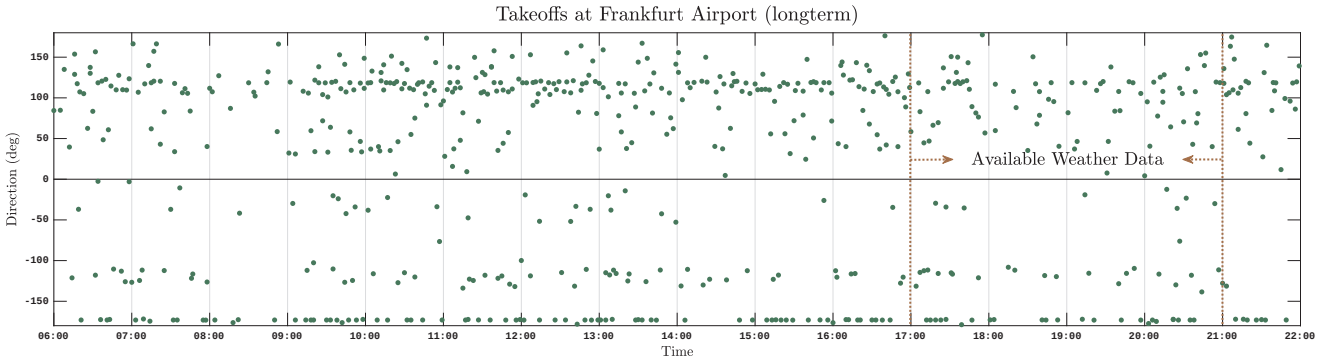

(f)

Figure 4: This figure depicts the takeoff and landing statistics of Munich airport and the takeoff statistics of Frankfurt airport. Every point marks a flight taking off or landing at that time with the respective flight direction (azimuth). The short term data (4a, 4b, 4c) takes into account the first two available data points of the flight paths. The resulting clusters indicate respective runways. The long term takeoff data (4d, 4f) shows the direction (relative to the airport) 15 to 20 minutes after takeoff. Respectively, the long term landing data (4e) depicts the descent direction.

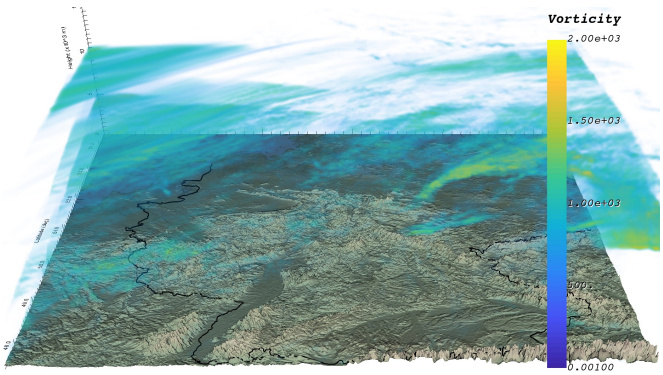

(a) Volume rendering of vorticity. Vorticity increases near the ground due to boundary-induced shear and at the tropopause (around 10 *km* altitude) due to wind shear between troposphere and stratosphere.

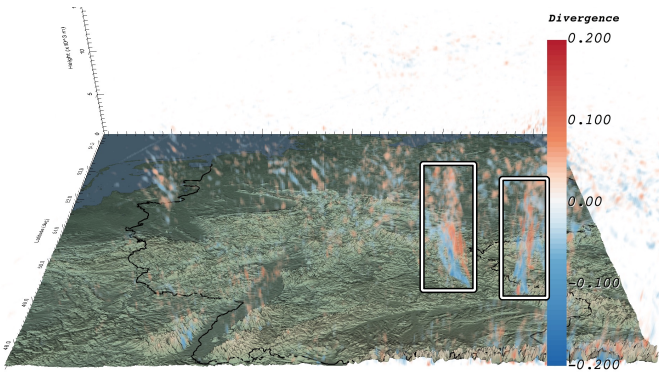

(b) Volume rendering of divergence. The highlighted regions show high convergence at the bottom and divergence higher up, which indicates updrafts.

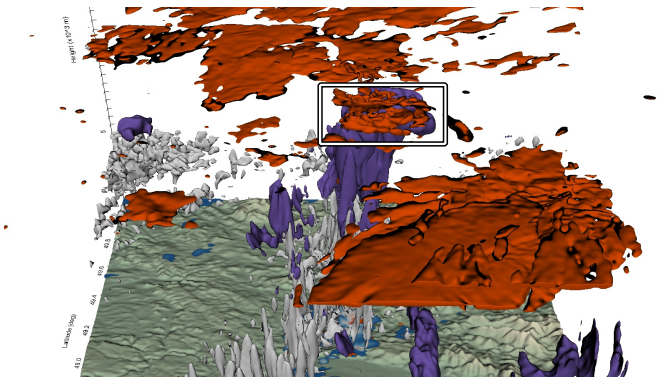

(c) Iso-surface of vorticity (red) together with CLW (white), CLI (violet) and precipitation on the ground in the *updraft* region. The vorticity present at the top of the cumulonimbus cloud is highlighted.

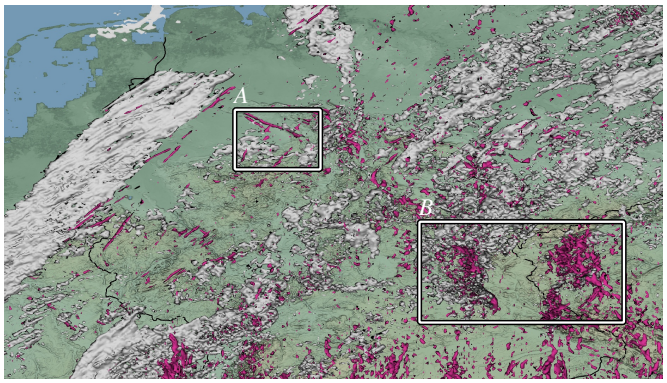

(d) Iso-surfaces of divergence and CLW reveal regions with divergence due to orography (*A*) and divergence following the updraft (*B*). Both regions are highlighed.

Figure 5: This figure relates updraft, vorticity and divergence to cloud attributes such as CLW and CLI.

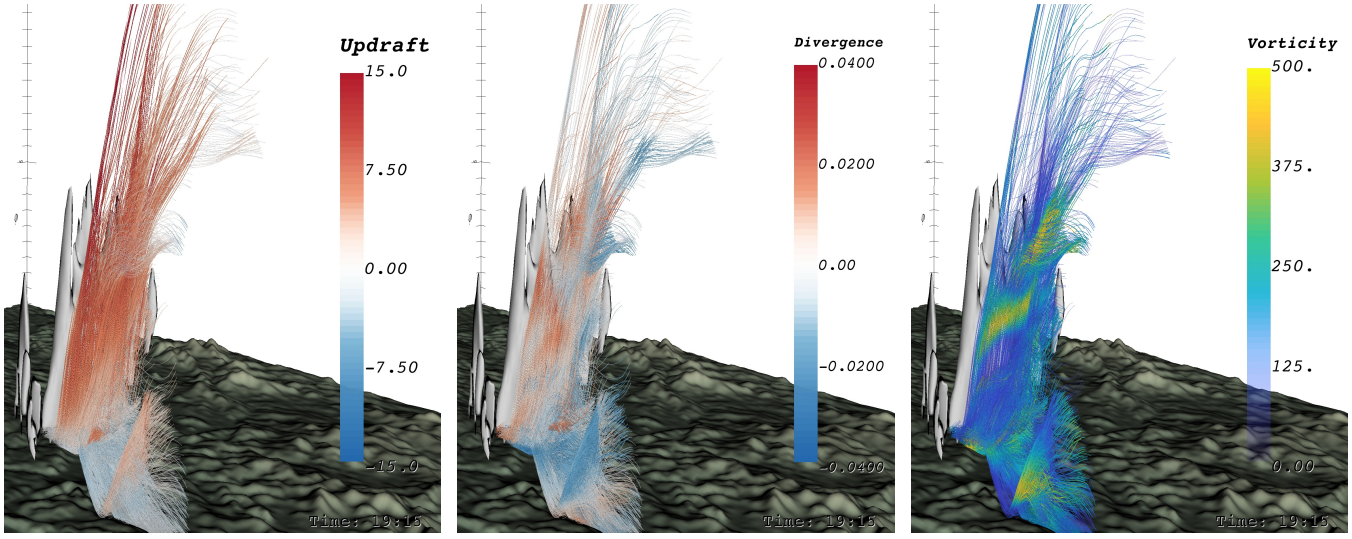

Figure 6: This figure shows 4000 pathlines seeded at the cloud bottom of the cumulonimbus cloud in south-east Germany. To prevent occlusion only a small iso-surface of the cloud water content ($CLW = 4 \times 10^{-4}\,\mathrm{kg\,kg^{-1}}$) is shown additionally. The pathlines were computed with a fourth-order Runge-Kutta integrator. The step size is 5 seconds and the underlying flow field has a temporal resolution of 1 minute.

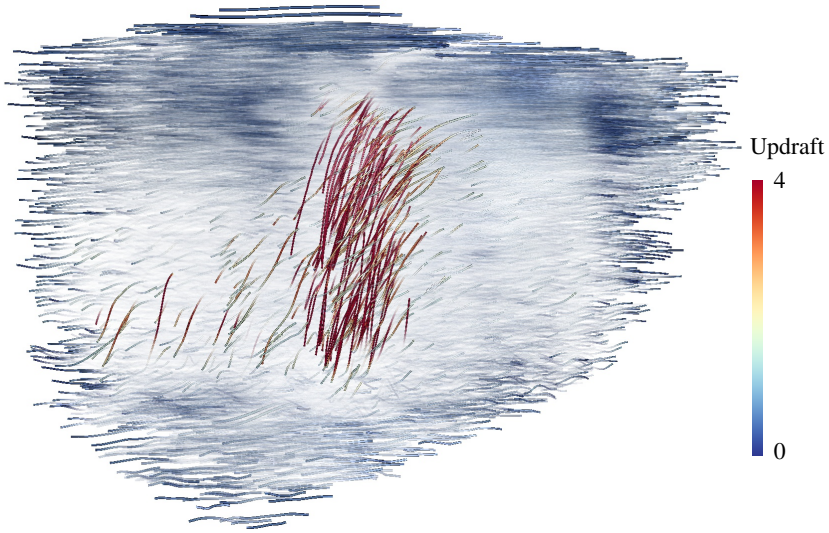

Figure 7: Focus and context visualization of pathlines in the *updraft* region. Using decoupled opacity optimization, opacities are adjusted so that trajectories with high updraft are visible, while the remaining pathlines are shown as context, which clearly indicates the updraft region. Here, the same region and time frame as in Fig. 6 is shown.

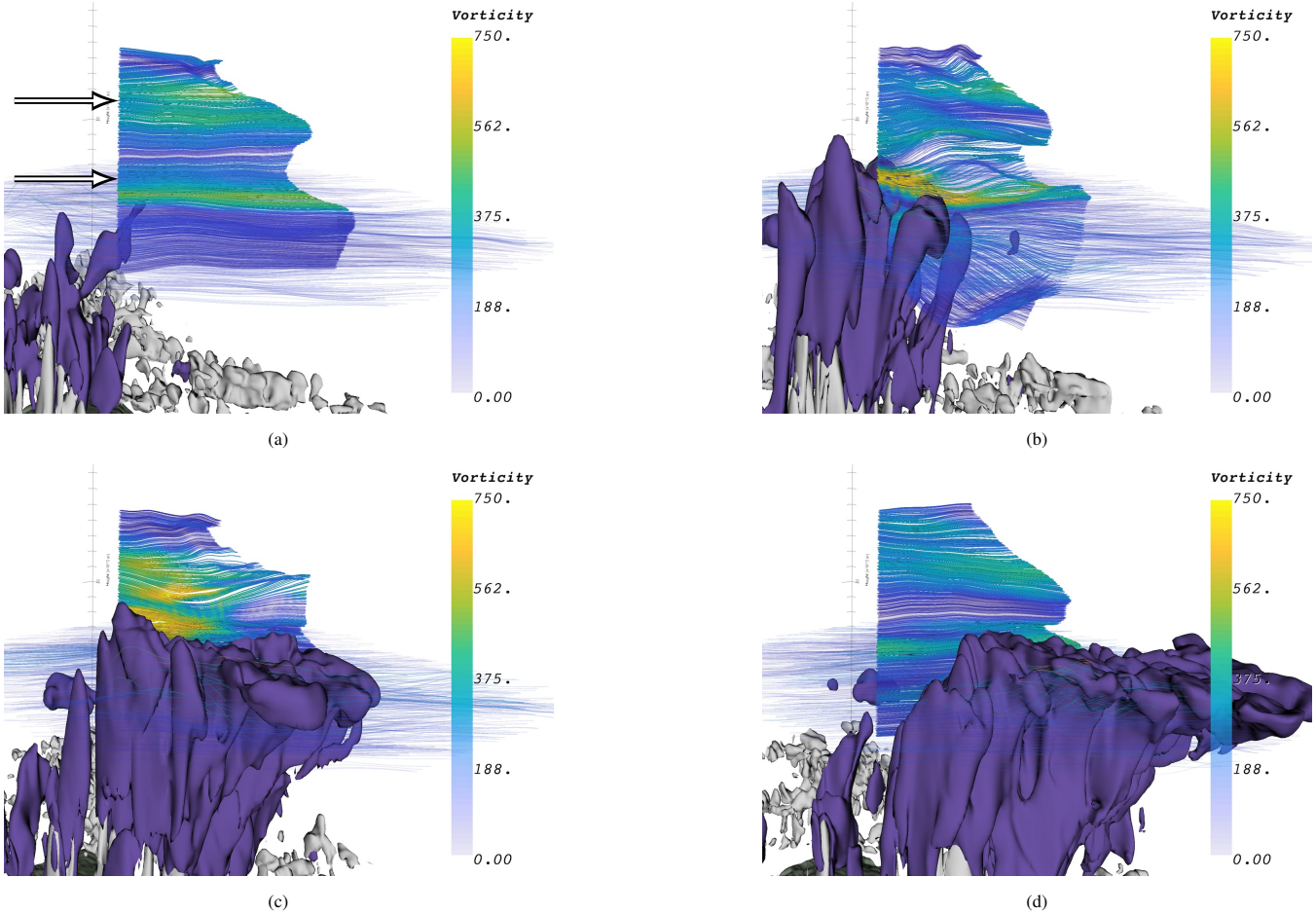

Figure 8: Visualization of the air flow in the *updraft* region around Regensburg. Pathlines at the top of the cloud are coloured by vorticity. The images show 15 minute intervals as the cloud moves by. In the first time step (a) the streaks of high vorticity are highlighted. They separate wind masses of different speeds, indicated by the length of the pathlines. While the cloud passes by (b and c), updraft causes turbulence that is visible in both the particle trajectories and the vorticity. Once the cloud has passed (d), the air flow pattern returns back to its original state.

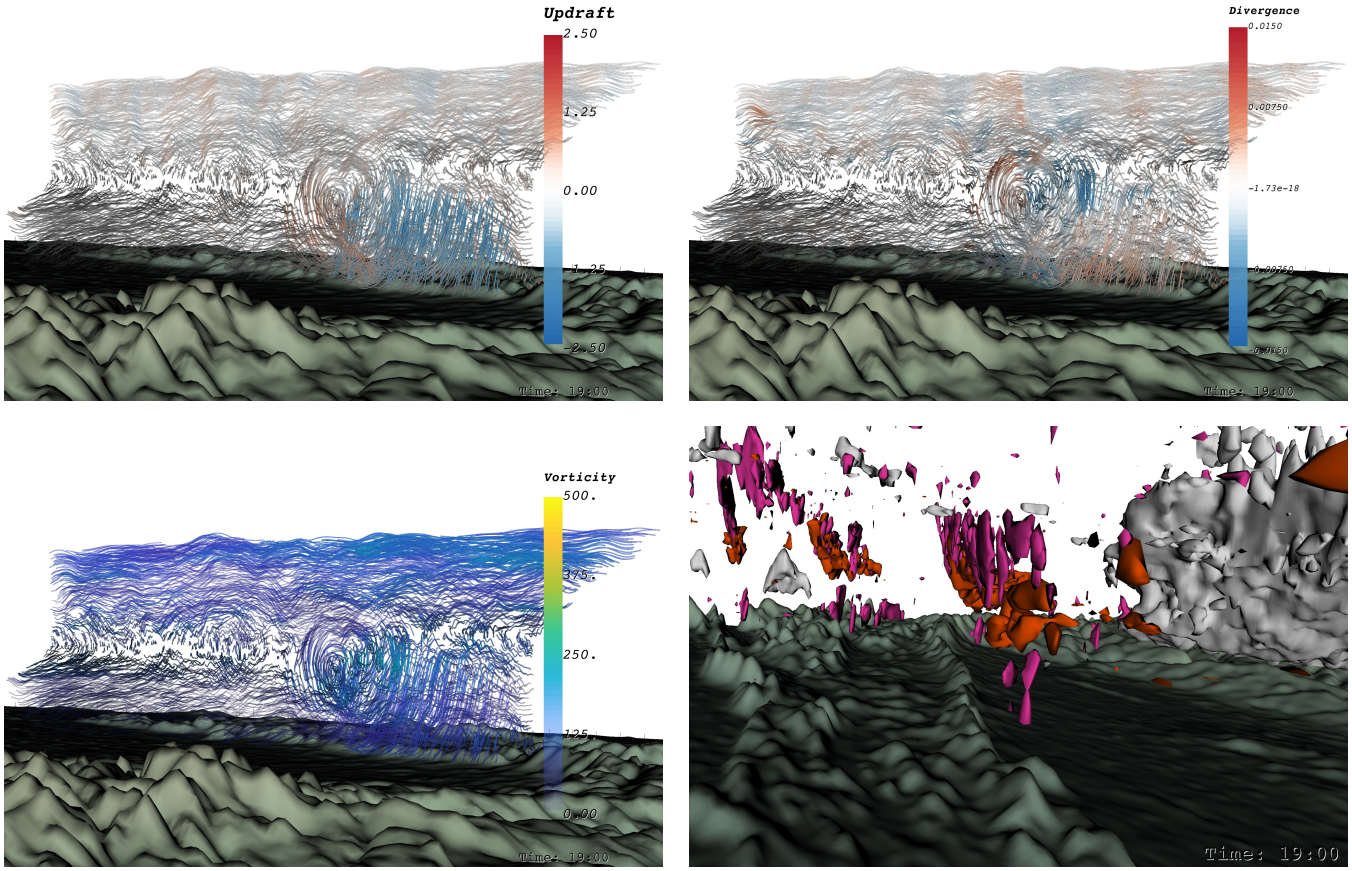

(a) The first three images show pathlines from 0 *km* to 3 *km* above the mountain range with updraft, divergence and vorticity color-coded on them, making an orography-induced updraft apparent. Further, iso-surfaces of vorticity (orange) and convergence (pink) appear in the same location. Here, for the thresholds $\|\nabla \times \mathbf{v}\| = 250$ and $\nabla \cdot \mathbf{v} = -0.007$.

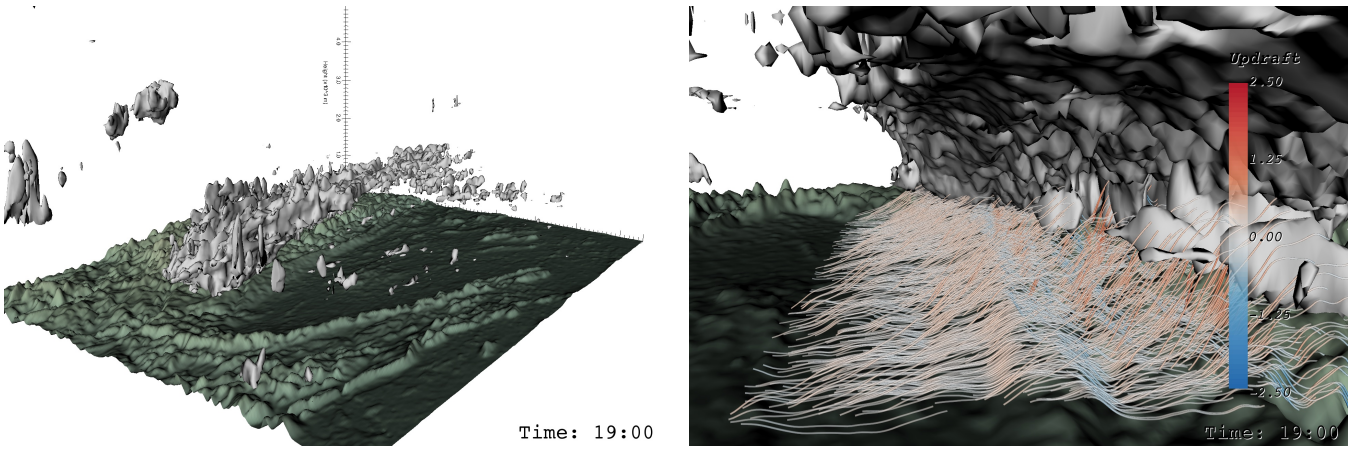

(b) Clouds, shown with CLW iso-surfaces ($CLW = 5 \times 10^{-4}\,\mathrm{kg\,kg^{-1}}$), line up along the mountain range (left). Pathlines indicate the forced updraft (right).

Figure 9: The Teutoburg Forest and the Egge Hills act as an obstacle that the arriving winds from the south-west have to climb up. This results in visible orography-induced turbulence and compression (a), as well as in a forced updraft with developing clouds (b).

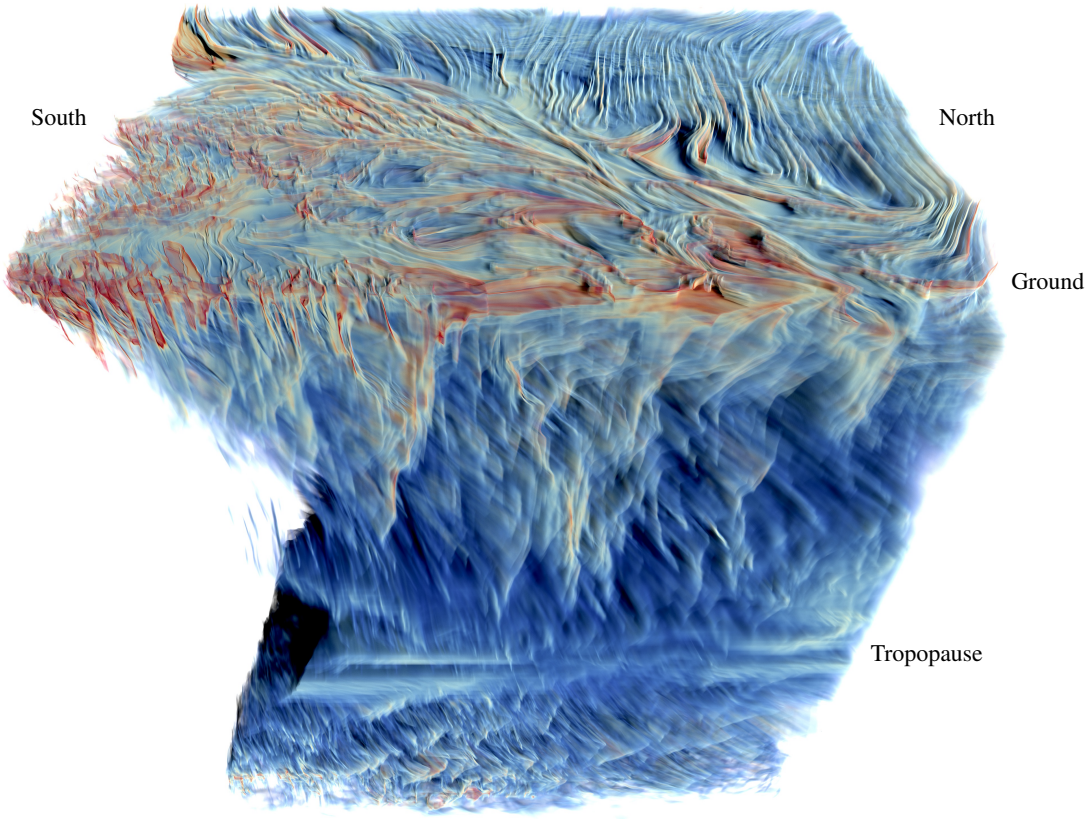

(a) Unbiased finite-time Lyapunov exponents (FTLE) for the atmospheric air flow above entire Germany.

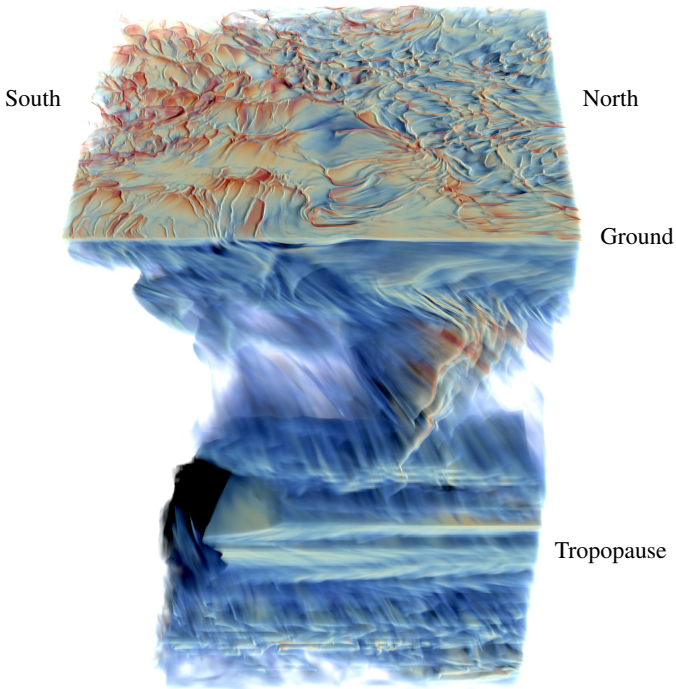

(b) Unbiased FTLE rendering for the *updraft* region around Regensburg.

Figure 10: Finite-time Lyapunov exponents (FTLE) are an indicator for hyperbolic Lagrangian coherent structures, which act as transport barriers in vector fields. In these visualizations, altitude is reversed (ground is at the top) and North is right. Both images show the turbulent movement near the ground and updraft columns towards higher altitude. The FTLE layer at high altitudes (bottom) is the tropopause.

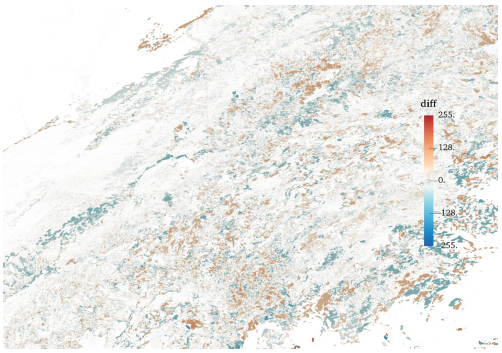

(a) Height of convective cloud base

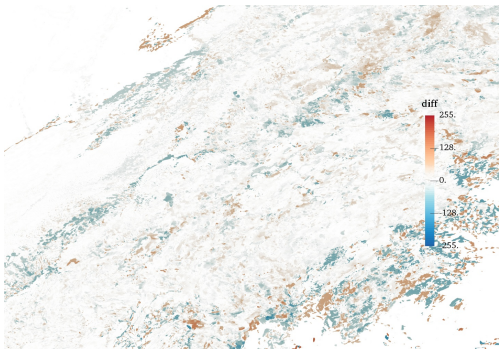

(b) Height of convective cloud top

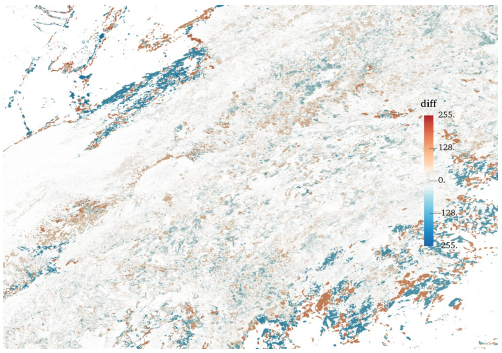

(c) Cloud base pressure

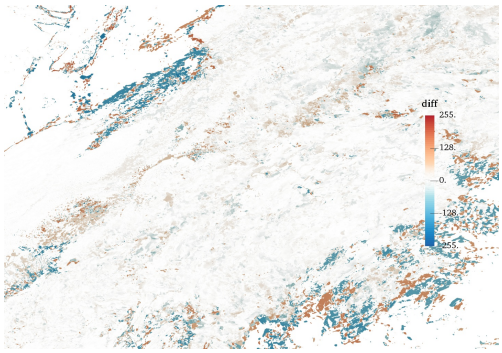

(d) Cloud top pressure

(e) CLW vertically integrated

(f) CLI vertically integrated

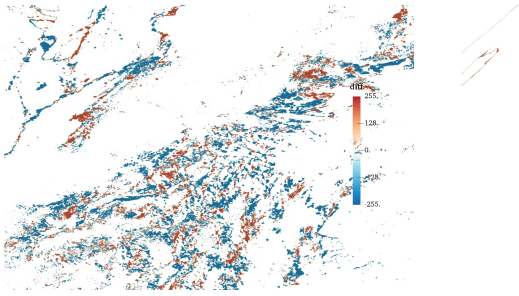

(g) Low level cloud cover

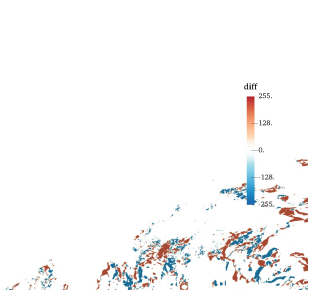

(h) Mid level cloud cover

(i) High level cloud cover

Figure 11: These visualization display the differences between the finest (Domain 3) and the coarsest (Domain 1) resolution of the original ICON data. Areas in which the Domain 1 (low resolution) has higher values are indicated blue. The other way around is indicated in red. Note that for height (11a and 11b) and pressure (11c and 11d) the difference maps are similar. For both, the differences at the cloud base (11a and 11c) are bigger than at the cloud top (11b and 11d). The differences for vertically-integrated measures are shown in Figs. 11e and 11f, which are remarkably small. Finally, the cloud cover differences are shown for three different altitudes in Figs. 11g, 11h and 11i, indicating that the greatest differences occur at low altitudes.

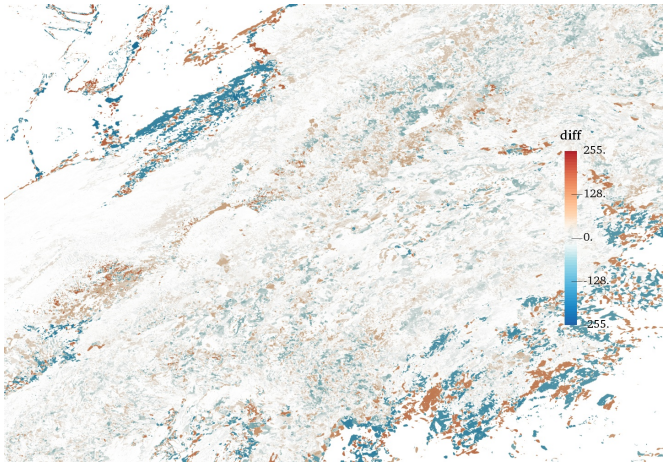

(a) Cloud base pressure difference from domain 1 to domain 3.

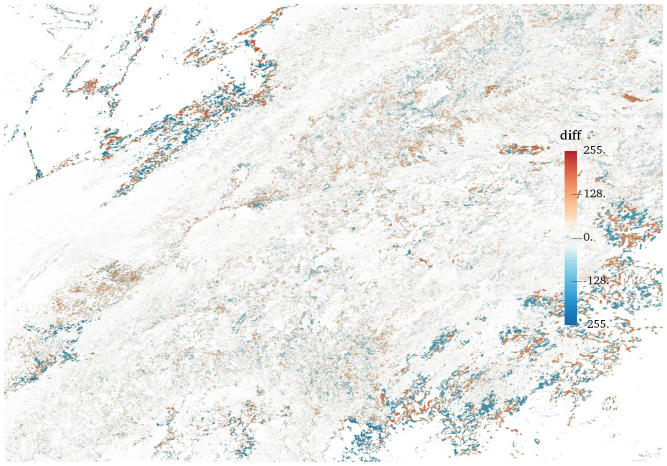

(b) Cloud base pressure difference from domain 2 to domain 3.

(c) CLIVI difference from domain 1 to domain 3.

(d) CLIVI difference from domain 2 to domain 3.

Figure 12: In this figure, the difference between all three resolutions of the original ICON data are visualized for two attributes, namely the cloud base pressure in Figs. 12a and 12b, and the vertically integrated cloud ice content (CLIVI) in Figs. 12c and 12d. The left side shows the differences between Domain 1 and Domain 3 as in Fig. 11. The right side shows the difference between Domain 2 and Domain 3. We see that Domain 2 is significantly more detailed than Domain 1, but still noticeable deviations are visible at cloud boundaries.

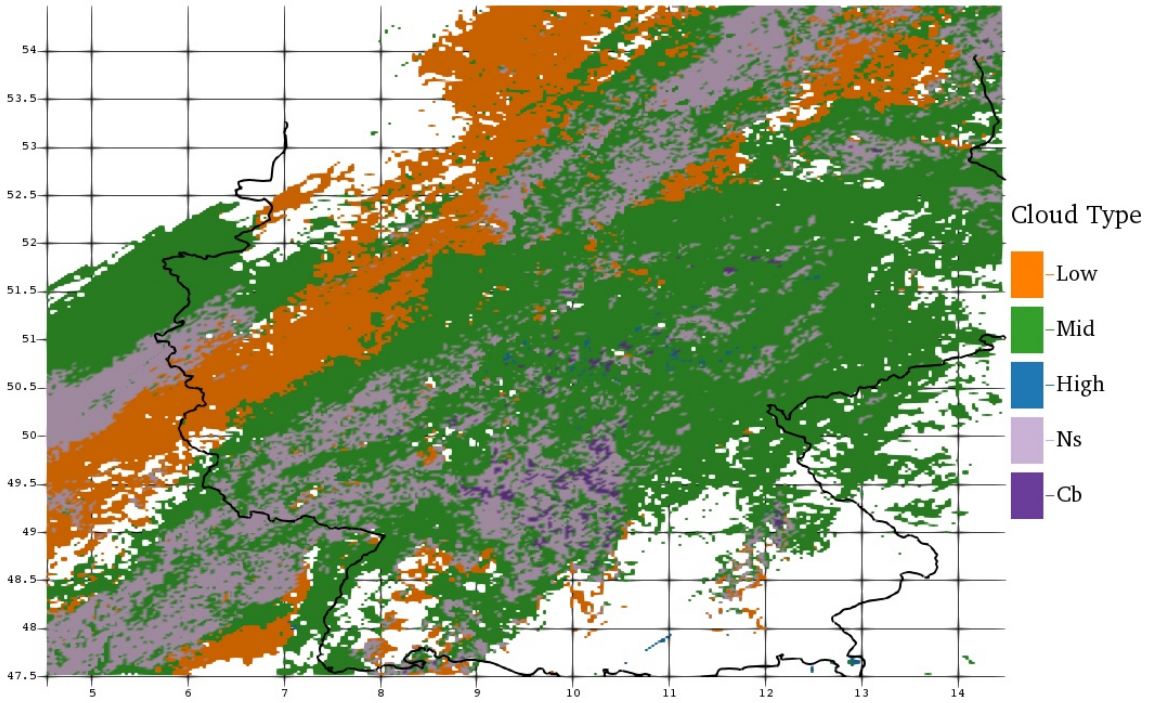

(a) Cloud classification using a basic scheme.

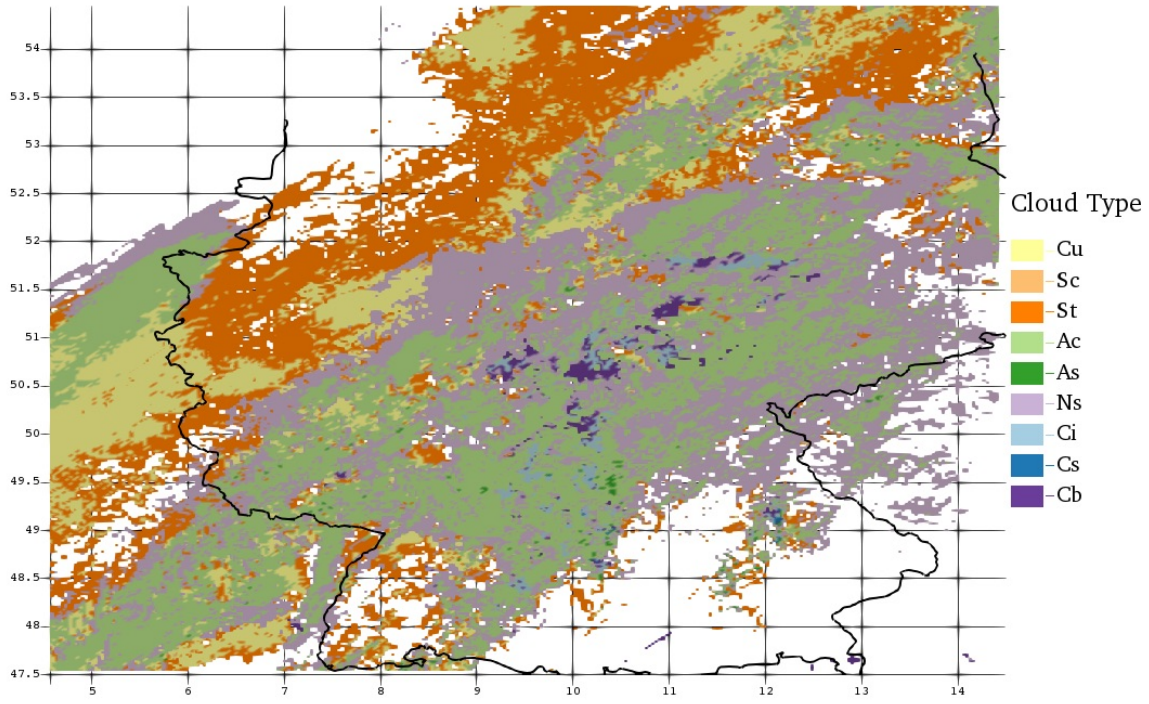

(b) Cloud classification using the ISCCP scheme.

Figure 13: Here, the results of the two classification schemes are shown. In Fig. 13a, clouds are mainly distinguished by height level and additionally nimbostratus (Ns) and cumulonimbus (Cb) clouds are detected. The second approach in Fig. 13b, which is based on the ISCCP classification scheme, distinguishes nine different cloud types. Low level clouds are split into cumulus (Cu), stratocumulus (Sc) and stratus (St). Mid level clouds are split into altocumulus (Ac) and altostratus (As). Finally, the high level clouds are split into cirrus (Ci) and cirrostratus (Cs). Note that the two approaches agree in most parts, except that the second approach seems to have lower thresholds for nimbostratus and cumulonimbus clouds.

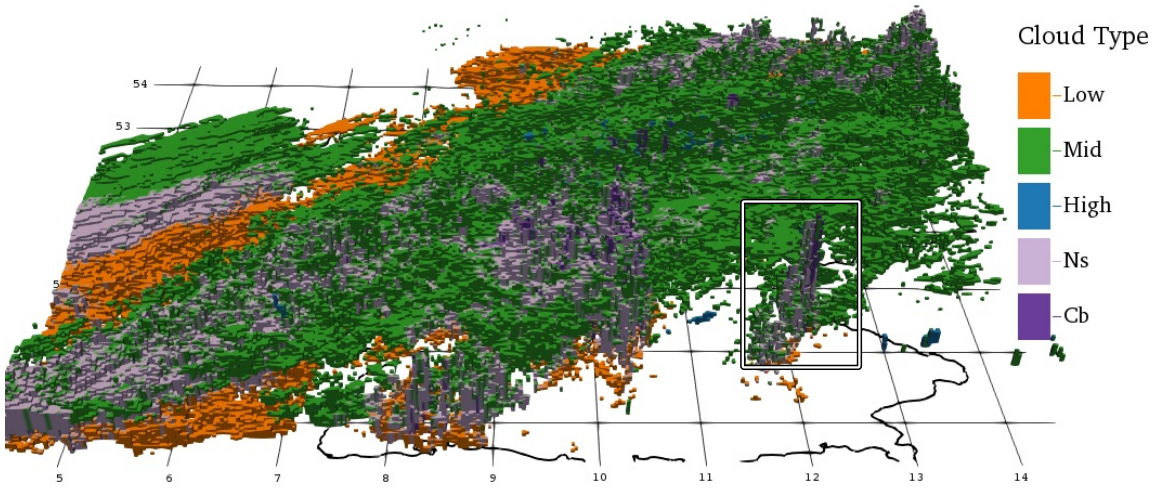

(a) Cloud classification using a basic scheme.

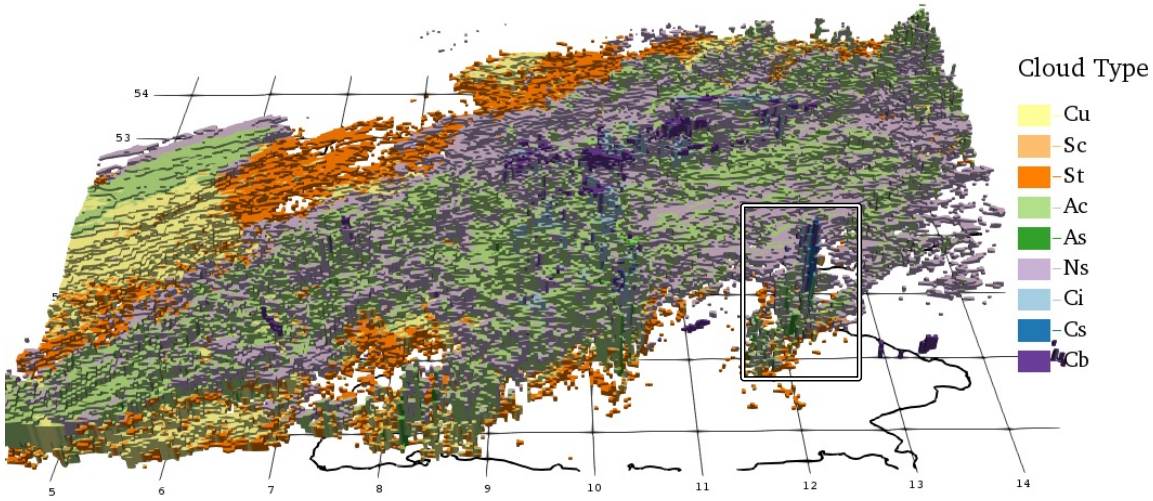

(b) Cloud classification using the ISCCP scheme.

Figure 14: A 3D visualization of the cloud classification results from Fig. 13 for the two classification schemes. Note how both approaches classify the clouds around Regensburg as a cumulonimbus cloud.